[Research Paper] 대한금속·재료학회지 (*Korean J. Met. Mater.*), Vol. 56, No. 10 (2018) pp.718-726
DOI: 10.3365/KJMM.2018.56.10.718

Effect of MgO Addition on the Monoclinic to Tetragonal Transition of ZrO_2 Fabricated by High Energy Ball Milling

Ashutosh Sharma and Byungmin Ahn*

Department of Materials Science and Engineering and Department of Energy Systems Research, Ajou University, Suwon 16499, Republic of Korea

Abstract: In this work, we studied the formation of partially stabilized zirconia by a high energy ball milling (HEBM) approach. Zirconia powder was mixed with 8 mol% MgO and the powder mixture was milled for 10 hours. The structural and morphological evolutions of the powder particles were studied using X-ray diffraction (XRD) and scanning electron microscopy (SEM), respectively. The Williamson-Hall method was used to calculate the crystallite size of the zirconia powder particles. The results show that the tetragonal zirconia phase (t-ZrO_2) can be very well stabilized after the addition of 8 mol% MgO. The formation of t-ZrO_2 was identified by XRD analysis after 3 hours of ball milling. In addition, SEM results demonstrated a great refinement in the size of the ZrO_2 particles whose distribution was in the sub-μm to nm range indicating better microstructural characteristics.

(Received July 18, 2018; Accepted August 16, 2018)

Keywords: ball mill, zirconia, microstructure, ceramics, crystallite size, strain

1. INTRODUCTION

Polymorphism in ceramics is an interesting topic in powder metallurgy, especially in zirconia, for several decades. Zirconia-based ceramics are widely in use due to their attractive electrical and mechanical properties as well as their high ionic conductivity at elevated temperatures with various applications in electrochemical cells, such as fuel cells, bio-implants, oxygen sensors and oxygen pumps [1-6]. Pure zirconia exhibits various polymorphs, i.e., a monoclinic (m-ZrO_2) phase at standard room temperature and pressure (STP) which transforms to tetragonal (t-ZrO_2) at around 1170 °C followed by a cubic fluorite structure (c-ZrO_2) at around 2370 °C before melting at 2716 °C [7]. Drastic volume changes (≈ 2.31%: c- → t-ZrO_2 and 4.5%: t → m-ZrO_2) associated with these transformations make the pure ZrO_2 unsuitable for industrial applications that require a compact structure. The t ↔ m-ZrO_2 transformation has important technological advantages because densified/fired structures may get easily transformed from tetragonal to monoclinic phases during cooling from firing temperatures (≈1300 – 1500 °C) [8]. This may result in a serious crumbling of the ceramic components into fine multi-grained powders.

Various studies attempted to prevent this t → m-ZrO_2 transformation by forming solid solutions or alloys of c-ZrO_2 with various dopants like MgO, CaO, La_2O_3, or Y_2O_3, in concentrations lower than that required for full stabilization of c-ZrO_2. By alloying with these oxides, the strained m-ZrO_2 phase at room temperature favors more symmetric metastable c* and t* lattice structures that are analogous to those in pure zirconia but have dopant ions substituted on Zr^{4+} sites and have a fraction of oxygen sites vacant to retain charge neutrality [9-12]. The crystal can be stabilized partially or fully, but partially stabilized zirconia (PSZ) has mechanical properties superior to those of fully stabilized zirconia, i.e., a low overall thermal expansion coefficient that counteracts the large thermal contraction of the c-ZrO_2 [13].

Garvie *et al*. pioneered PSZ stabilized by dopants (such as Y_2O_3, Al_2O_3, CeO_2, CaO, Cu, Sr, Mg, etc.), which generated great technological interest in the development of new materials, as ZrO_2-$A1_2O_3$ or ZrO_2-mullite composites [14-22]. Among these, magnesium-based ceramics are the most interesting in the ceramic industry in view of their strength

*Corresponding Author: Byungmin Ahn
[Tel: +82-31-219-3531, E-mail: byungmin@ajou.ac.kr]

and fatigue properties [23-26]. Magnesium partially-stabilized zirconia (Mg-PSZ) exhibits strong R-curve behavior due to transformation toughening with peak fracture toughness up to 20 $MPam^{1/2}$ [14,24-26]. The underlying mechanism is the stress-induced t → m-phase transformation. The key to getting good fracture toughness in Mg-PSZ is to maximize the amount of transformable tetragonal phase by eutectoid and/or sub-eutectoid aging treatment and an optimized cooling rate [14,23-26].

There are various well-established methods for the synthesis of zirconia: wet chemical methods, plasma spraying, high energy ball milling (HEBM), pulsed laser deposition, laser evaporation-condensation, and hot isostatic pressing [27]. However, HEBM has its own additional advantages. For example, it is simple, easy, economical, and environmentally friendly. Such ball milled powders are generally homogeneous in composition, very reactive and able to be sintered at lower temperatures than those usually employed, and they yield materials with higher density and improved mechanical and electrical properties [27,28]. It has been shown that dual phase MgO-ZrO_2 ceramics have excellent thermal conductivity for various applications [26]. This paper describes the results of our experiment to fabricate dual phase magnesia-zirconia ceramics. In this study, we synthesized the zirconia stabilized by 8mol% MgO by the mechanical milling approach. The Williamson-Hall Method was employed to determine the crystallite size and lattice strain of the zirconia and morphological characterizations were carried out.

2. EXPERIMENTAL DETAILS

2.1 Materials

Magnesium oxide (MgO, 99.8% purity) and zirconium oxide (monoclinic, 99.9% purity) were procured from Sigma Aldrich, USA. The compositions are given in Table 1.

Table 1. Sample compositions.

S. No.	Material	Composition (mol%)
1	ZrO_2	92
2	MgO	8

2.2 Method

A mixture of 8 mol% MgO and 92 mol% ZrO_2 was prepared and subjected to HEBM for 10 h in a ball mill (Fritsch Pulverissette P-4 planetary, GmbH, Germany). Around 1.1 g of MgO and 38.8 g of ZrO_2 was weighed for a 40 g batch and mixed thoroughly in a HEBM machine with WC balls and vials. The employed HEBM and the schematic diagram of the ball milling phenomena are shown in Fig. 1(a) and (b).

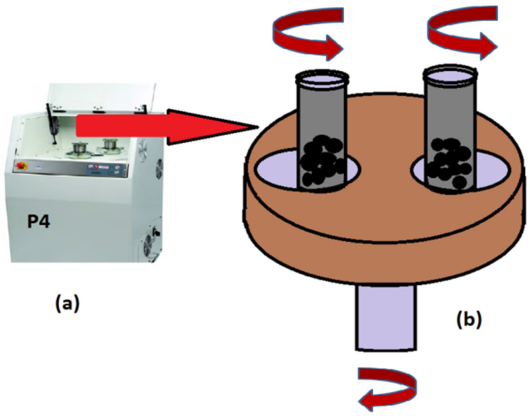

Fig. 1. (a) P4-planetary ball mill apparatus and (b) Schematic depicting the ball motion inside the ball mill.

The centrifugal force produced by the vials rotating around their own axes and the force produced by the rotating support disk both act on the vial contents, which consists of the material to be ground and the grinding balls. Since the vials and the supporting disk rotate in opposite directions, the centrifugal forces alternately act in opposite directions [27,28]. This causes the grinding balls to run down the inside wall of the vial, the friction effect, followed by the material being ground and grinding balls lifting off and traveling freely through the inner chamber of the vial and colliding against the opposing inside wall, the impact effect [28]. The ball to powder weight ratio was ≈ 10:1, and toluene was used as a process control agent. The samples were obtained at 0, 1, 3, 5, and 10 h.

2.3 Characterization studies

The samples thus obtained were characterized for their phase identification and crystallite size by a Bruker's X-ray diffractometer with a Co target operating at 40 kV and 30 mA. The X-ray diffraction pattern was further analyzed using Philips X'pert software applications.

The morphology of the powders was determined from the JEOL scanning electron microscope (SEM). Energy dispersive X-ray analysis (EDS) was carried out to examine the

corresponding elemental distribution. The crystallite size and lattice strain of the powder particles were determined from the X-ray peak broadening as per the Williamson-Hall Method as follows. In general, the X-ray diffraction peaks are broadened due to the instrumental effects, the crystallite size, and the R.M.S. strain in the material. Structural broadening for the calculation of crystallite size is obtained using the relation:

$$\beta^2 = \beta^2_{observed} - \beta^2_{standard} \quad (1)$$

where $\beta_{standard}$ and $\beta_{observed}$ are the full width at half maximum of any particular reflection from the standard silicon disc and the powder, respectively, and β is the full width at half maximum of the particular reflection peak. The crystallite size analysis was done by the Williamson-Hall method. This method assumes that both the size and strain broadening of profiles follow Lorentzian distribution [29]. According to this assumption, the mathematical relationship involving the integral breadth (β), the volume weighted average crystallite size (D_v) and the lattice strain (ε) can be given as

$$\frac{\beta\cos\theta}{\lambda} = \frac{1}{D_v} + 2\varepsilon\left(\frac{2\sin\theta}{\lambda}\right) \quad (2)$$

The plot of $\left(\frac{\beta\cos\theta}{\lambda}\right)$ versus $\left(\frac{2\sin\theta}{\lambda}\right)$ gives the value of the lattice strains from the slope and crystallite size from the ordinate intercepts.

Further, to examine the particle size and distribution, transmission electron microscope (TEM, Philips G20 Twin, USA) was employed operating at 200 kV. The as-prepared powders were subjected to ultrasonic vibration in ultrasonicator (Labsonic M) in ethanol for 2 h and drop coated carbon grids for examination.

3. RESULTS AND DISCUSSION

3.1 XRD analysis

The X-ray diffraction profile was plotted for different hours of ball milling as shown in Fig. 2.

The X-ray diffraction data revealed that with an increasing milling time the crystallite size of the powder decreased gradually as the peaks became broader. At a 2-theta value of 28.15°, the peak in the 0 h sample confirmed the presence of m-ZrO_2 [30]. With an increase in the milling time above 3 h, the presence of tetragonal phase was detected [31]. As the

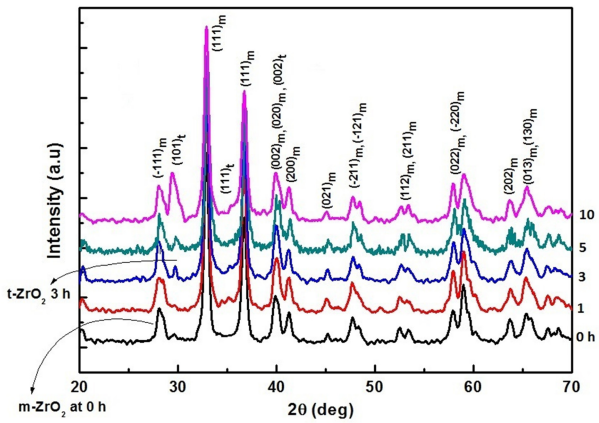

Fig. 2. X-ray diffraction pattern of the samples.

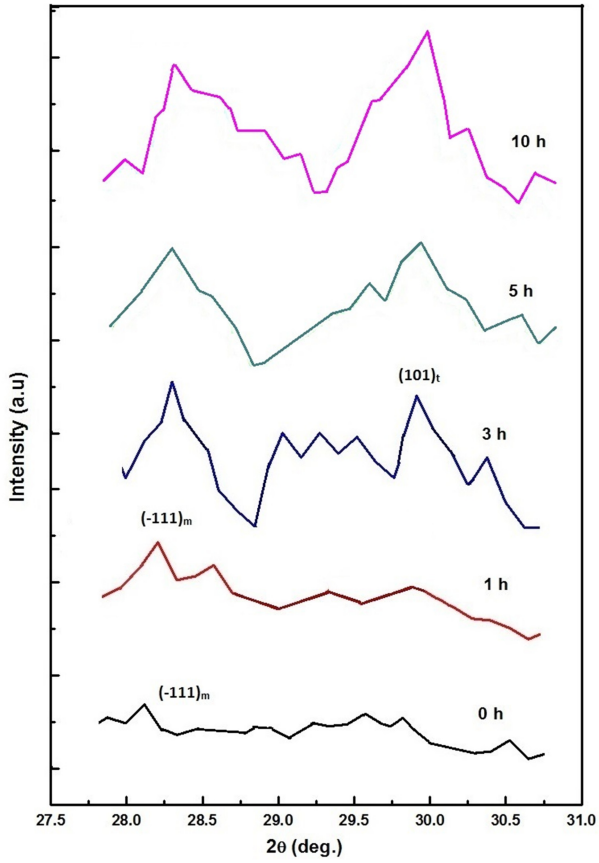

Fig. 3. Process of tetragonality in zirconia phase with ball milling duration. The tetragonal phase of zirconia is confirmed at 3 h ball milling and it becomes more prominent as the time of milling increases.

milling time increased, the tetragonal phase became more prominent, which is evident from the splitting of the peak as the milling time increased. A closer view of the peaks around 2-theta of 28°-30° are presented in Fig. 3. The average

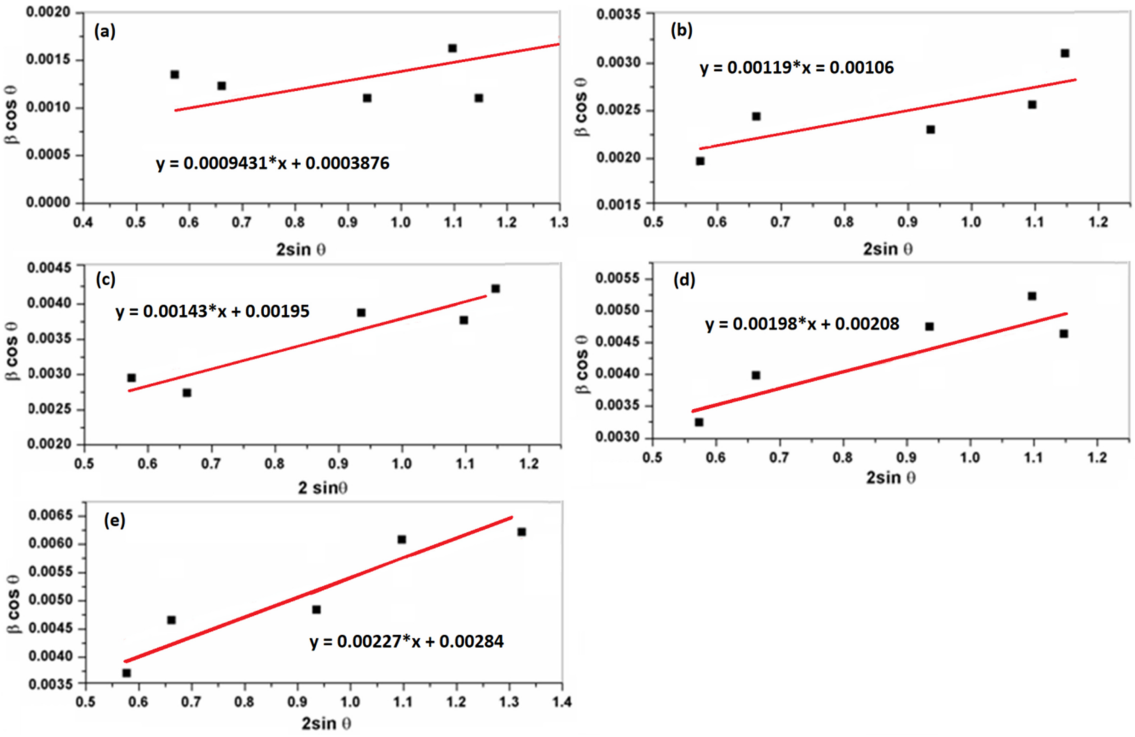

Fig. 4. Williamson Hall plot of ZrO_2 powder subjected to (a) 0, (b) 1, (c) 3, (d) 5, and (e) 10 h of HEBM.

crystallite size was also determined using these data. For as-received zirconia powder (0 h ball milled sample), the average crystallite size was in the sub-micrometer range. This value went on decreasing as the milling time increased and reached the nanometer range.

3.2 Crystallite size determination

Figure 4 shows the Williamson Hall plot of ZrO_2 powders prepared by the HEBM. The crystallite size and lattice strain of ZrO_2 powders were calculated from the intercept and the slope of the Williamson Hall plot, respectively.

The crystallite size and lattice strain calculated from the Williamson Hall method for different ball milled samples are given in Table 2. The average crystallite size was 28 nm for the 10 h ball milled sample.

Table 2. Crystallite size and lattice strain of ZrO_2 powder as obtained from the Williamson-Hall method

S.No.	Milling time (h)	Crystallite size (nm)	Lattice strain ($\times 10^{-3}$)
1	0	210	0.54
2	1	76	0.67
3	3	42	0.71
4	5	37	1.03
5	10	28	1.29

The crystallite size reduction was due to the repeated fracturing and cold-welding of particles in the course of milling. The formation of defects during the collision process of the powder particles, the reduction of crystallite size of the powder mixture, and the increase in lattice strain caused a lowering of the activation energy and increased the diffusivity of the system. This resulted in the stabilization of the tetragonal phase at higher milling times. It was revealed that the crystallite size decreased from 210 to 28 nm and the lattice strain increased from 0.4×10^{-3} to 1.29×10^{-3} with the increase in milling time [32]. In general, longer milling times causes a finer grain size and large lattice strain. Increasing lattice defects and a decreasing size of m-ZrO_2 are the two main driving forces for the m→ t-ZrO_2 transformation. These factors raise the internal energy of the milled powder, which is relatively comparable to that of high-temperature conditions where t-ZrO_2 becomes stable, i.e., 10 h of ball milling. Similar behavior was also noticed by Chen *et al*. in the past [33]. On the other hand, the magnitude of the increase in temperature during the milling process was too low ~100-

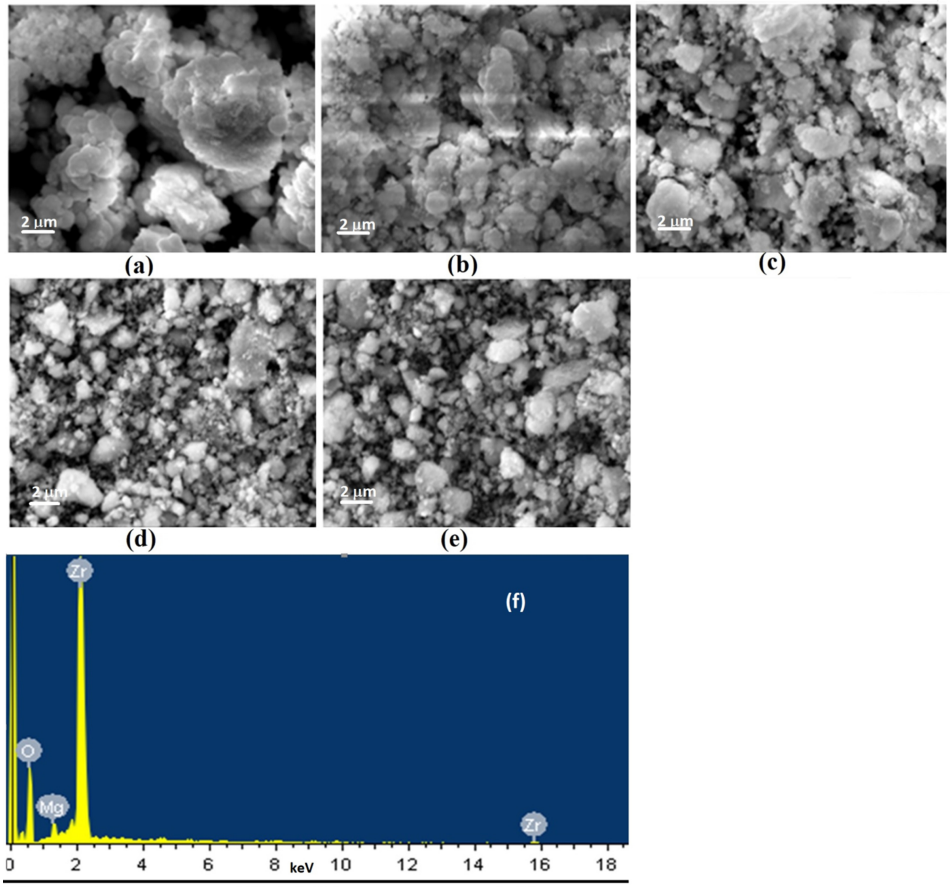

Element	Weight%	Atomic%
O K	39.69	77.76
Mg K	1.60	2.07
Zr L	58.71	20.18
Totals	100.00	

Fig. 5. (a) SEM images of ball milled zirconia samples at different milling times of (a) 0, (b) 1, (c) 3, (d) 5, and (e) 10 h, and (f) EDS analysis of the sample

200 °C to drive the m→ t-ZrO_2 transition. Therefore, it seems almost impossible to form t-ZrO_2 in the given conditions. However, it is well established that the addition of oxide dopants, such as calcia or magnesia, reduces the temperature gap in the m → t-ZrO_2 phase transition [34].

In other words, the solid solution of m-ZrO_2 ~ [m-ZrO_2(SS)] can transform to a solid solution of t-ZrO_2 ~ [t-ZrO_2(SS)] at a very low temperature. Annamalai *et al*. found that [m-ZrO_2(SS)] transforms to [t-ZrO_2(SS)] by the heat of grinding friction in Y_2O_3 and CeO_2 stabilized t-ZrO_2 crystals. They demonstrated that the temperature increase during the HEBM process seems to be of the same order as that induced by grinding [35]. These arguments suggest that some magnesia got dissolved in the m-ZrO_2, forming [m-ZrO_2(SS)] before 3 h, and the [m → t-ZrO_2(SS)] transition took place by the heat of the milling. Therefore, the tetragonal phase should be designated as [t-ZrO_2(SS)].

3.3 Morphology of zirconia powders

SEM photographs of the samples were taken for all the samples at different hours of ball milling. The scanning electron micrographs are shown in Fig. 5. It clearly shows that the crystallite size decreased as the milling time increased and how the morphology was changing continuously. By careful observation of the photographs of the samples at low magnification, it can be seen that the

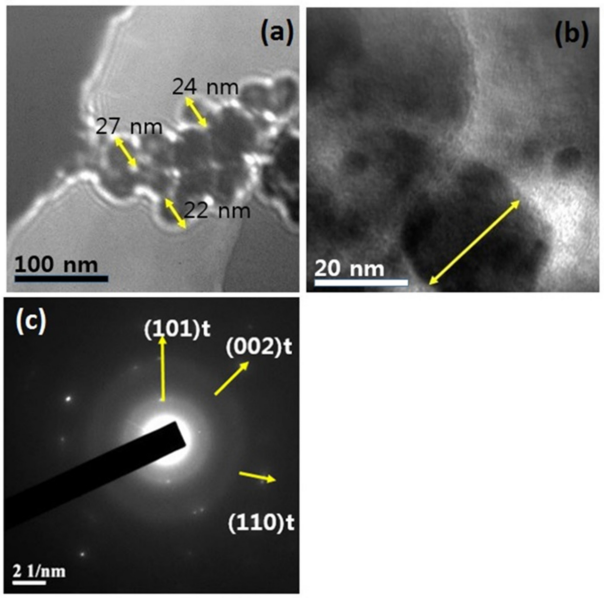

Fig. 6. (a) TEM bright field images of zirconia powder milled for 10 h, (b) high-resolution image of (a), and (c) selected area diffraction pattern of (a).

crystallite size of the 10 h ball milled sample was greater than the size of the 5 h ball milled sample. This can be due to the agglomeration of the particles from long hours of ball milling [36,37]. The average crystallite size for 0 h ball milling was in the micrometer range, whereas for the 10 h ball milling sample, the average crystallite size was 28 nm. The elemental composition of the samples is given by the following EDS analysis as shown in Fig. 5. The observed sample shows the presence of MgO is successfully achieved in the ZrO_2 matrix.

A more clear shape and distribution of zirconia powders is seen in the TEM image of the 10 h ball milled sample (Fig. 6). The particle size is around 22 nm at high resolution, which confirms the XRD results (Table 2). The selected area diffraction pattern further confirms the tetragonality in the zirconia particles.

Based on the observations, the phase transition process is given as:

$$\text{m-}ZrO_2 + MgO \rightarrow [\text{m-}ZrO_2(SS)] + MgO \rightarrow [\text{t-}ZrO_2(SS)] + MgO \rightarrow [\text{c-}ZrO_2(SS)] \quad (3)$$

It can be inferred that HEBM is an important means to tailor zirconia-based ceramics and can possibly produce some novel microstructures.

3.4 Theory of zirconia stabilization

The first observation of the m → t-ZrO_2 transformation during vibratory type milling was noticed in 1972 [38]. It was found that when a sufficiently small particle size of ZrO_2 reached ≈10-30 nm, the m-phase transforms to the t-phase. It was shown that the surface energy excess, i.e., the difference in surface energy between m- and t-ZrO_2 accounted for the phase transformation. In particular, lower surface energy is of the tetragonal transition rather than the monoclinic one. According to thermodynamics, in general, for the stability of the tetragonal phase [39], we have

$$G(t) + S(t)\gamma(t) + V(t) < G(m) + S(m)\gamma(m) + V(m) \quad (4)$$

where G is the free energy of a zirconia crystal (cal/mol), V is the strain energy (cal/g); γ is the surface free energy (cal/cm^2) and S is the specific surface area (cm^2/mol). For spherical particles S = 6/ρD. Here ρ and D are the density and particle diameter, respectively. Equation (4) can be rewritten as:

$$G(t) + 6\,\gamma(t)/\rho(t)\,D + V(t) < G(m) + 6\,\gamma(m)/\rho(m)\,D + V(m) \quad (5)$$

The critical diameter Dc below which particles will transform to tetragonal phase is given by

$$Dc = 6/[(G(t) - G(m) + (V(t) - V(m)] \times [(\gamma(m)/\rho(m) - \gamma(t)/\rho(t)] \quad (6)$$

Assuming the surface energy exceeds the lattice strain energy, we have V → 0. Substituting the various values for zirconia: γ(m) = 1130 ergs/cm^2 [40]; γ(t) = 770 ergs/cm^2 [41]; G(t) – G(m) = 1213 cal/mol (at 28 °C) [42]; ρ(t) = 5.86 g/cm^3 and ρ(m) = 5.74 g/cm^3 [43,44]. Dc comes out to be ≈ 10-30 nm, which indicates that a complete tetragonal phase would be achieved when the average diameter of particles would be 10-30 nm.

According to the study of Patil and Subbarao [45], the m-ZrO_2 phase changes to t-ZrO_2 by the movement of an interface parallel to the (001) plane. The orientation relations in the ZrO_2 phase transition are given by the following equations:

Movement of Planes: (100)m ‖ (110)t, and (7)

Movement in Directions: [010]m ‖ [001]t. (8)

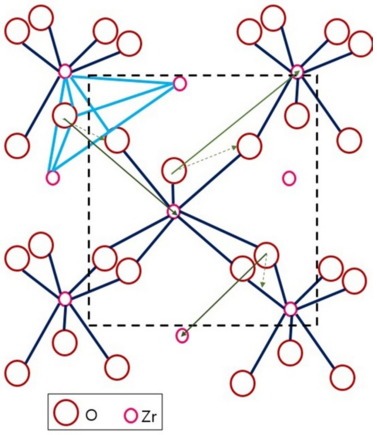

Fig. 7. Monoliclinic crystal structure of ZrO_2. The layer of ZrO_7 groups at x = 1/4 projected on (100)m plane. The dark blue crosses show the oxygen positions in tetragonal form. One O_IZr_3 polyhedra is highlighted in sky blue. The green line shows the probable movement of oxygen while dotted green line shows its direction of movement. The square outline shows the position of unit cell at x = 0 [45].

In monoclinic ZrO_2, the Zr atom is surrounded by the 7 oxygen atoms $O_{II}{}^m$ (at 2.189, 2.220, 2.151, and 2.285 Å), and 3 oxygen atoms $O_I{}^m$ (at 2.057, 2.163, and 2.051 Å) [45]. This irregular network changes to tetragonal form where Zr atom is surrounded by 8 oxygen atoms, for oxygen atoms $O_{II}{}^t$ at 2.455 Å and four $O_I{}^t$ at 2.065Å as shown in Fig. 7.

From the orientation relationship, it becomes clear that $O_{II}{}^m$ atoms move in the (200)m plane, and thereby two of them come nearer to the central Zr atom while the other two go farther from it. In other words, two of them become $O_I{}^t$ and the other two $O_{II}{}^t$. In the $O_I{}^m$ polyhedron two $O_I{}^m$ atoms become $O_I{}^t$ and the third $O_I{}^m$ atom becomes $O_{II}{}^t$. However, it should be mentioned that not only $O_I{}^m$ atoms but also the atoms Zr and $O_{II}{}^m$ undergo substantial movements. All these changes result in eightfold coordination for Zr and fourfold coordination for all oxygen atoms.

When the dopant oxides (i.e., 8 mol% MgO) are added, it prevents the formation of m-ZrO_2 by increasing the lattice strain contribution and stabilizing the tetragonal form, called partially stabilized zirconia, while the electrostatic neutrality of the ionic material is maintained by creation of oxygen vacancies. In other words, the substitution of Zr^{4+} by Mg^{2+} is compensated for by the presence of interstitial cations or anionic vacancies. The oxygen vacancies form as per the following equation [46,47]:

$$MgO \rightarrow Mg''_{Zr} + O^x_o + V_o^{oo} \quad (9)$$

Here, Mg''_{Zr} is Mg^{2+} which occupies the Zr position in the lattice, O^x_o is the oxygen on the anion lattice in ZrO_2 and V_o^{oo} is the oxygen vacancy with two plus charges. The vacancy concentration is equal to the Mg^{2+} ion concentration. According to the tight binding model developed by Stefano *et al*. [46], a possible explanation of the stabilization mechanism is that when the concentration of O^x_o vacancies is higher than 8 mol% MgO, the ZrO_2 crystal transforms to the fully stabilized cubic fluorite structure. However, when the concentration of dopants is very low, (< 8 mol% MgO), producing fewer oxygen vacancies, a relatively large volume of zirconia crystal is left in the fluorite structure while it transforms to tetragonal form. During this distortion, due to the simultaneous coordinated motion of all the oxygen, the vacancies are dragged along the tetragonal distortion of the oxygen sublattice. In other words, as seen from the figure, the O^{2-} ions are shuffled (pulled upwards and compressed downwards) from their position, resulting in the tetragonal distortion in crystals.

4. CONCLUSIONS

High energy ball milling is an effective process for preparing partially stabilized zirconia. This study demonstrated that partial stabilization of zirconia can be successfully achieved with 8 mol% concentration of MgO after ball milling for 10 h. The XRD results show that the monoclinic to tetragonal phase transformation begins at 3 h and is fully completed at 10 h of ball milling. The average crystallite size in the nanometer range can be easily achieved by this process for better microstructural properties. The Williamson-Hall method of XRD analysis indicated an average crystallite size of 28 nm with a lattice strain of 1.29×10^{-3}. The TEM analysis showed that the particle size of tetragonal zirconia after 10 h milling was around 22 nm. We concluded that the addition of dopant oxides (MgO) creates a crystalline field around m-ZrO_2 that reduces the volume of the m-ZrO_2 causing destabilization of the m-ZrO_2 and leading to the formation of t-ZrO_2.

ACKNOWLEDGEMENTS

This research was supported by Basic Science Research

Program through the National Research Foundation of Korea (NRF) funded by the Ministry of Education (NRF-2018R1D1A1B07044481) (B.A.). This research was supported by Basic Science Research Program through the National Research Foundation of Korea (NRF) funded by the Ministry of Education (NRF-2018R1D1A1B07044706) (A.S.).

REFERENCES

1. J. Nowotny, *Science of Ceramic Interfaces II*, 1st ed., pp. 71-110, Elsevier Science, Amsterdam (1994).
2. J. R. Kelly and I. Denry, *Dent. Mater.* **24**, 289 (2008).
3. W. D. Kingery, H. K. Bowen, and D. R. Uhlmann, *Introduction to Ceramics, 2nd ed*., Wiley-Interscience, New York (1976).
4. Il. H. Bang and S. Y. Cho, *Korean J. Met. Mater.* **55**, 819 (2017).
5. J. S. Lee, M. J. Lee, T. Y. Lim, Y. Lee, D. W. Jeon, S. K. Hyun, and J. H. Kim, *Korean J. Met. Mater.* **55**, 290 (2017).
6. G. B. Ahn, K. H. Choe, S. S. Kim, and G. S. Cho, *Korean J. Met. Mater.* **54**, 559 (2016).
7. A. G. Evans and A. H. Heuer, *J. Am. Ceram. Soc*. **63**, 241 (1980).
8. A. H. Heuer, *J. Am. Ceram. Soc*. **70**, 689 (1987).
9. A. H. Heuer, N. Claussen, W. M. Kriven, and M. Ruhle, *J. Am. Ceram. Soc.* **65**, 642 (1982).
10. W. E. Lee and W. M. Rainforth, *Ceramic microstructures, Property Control by Processing*, pp.317-387 and 509-570, Chapman and Hall, London (1994).
11. I. J. Shon, J. K. Yoon, and K. T. Hong, *Met. Mater. Int*. **23**, 940 (2017).
12. H. W. Park, J. W. Jang, Y. J. Lee, J. H. Kim, D. W. Jeon, J. H. Lee, H. J. Hwang, and M. J. Lee, *Met. Mater. Int.* **23**, 1227 (2017).
13. B. Mondal, A. N. Virkar, A. B. Chattopadhyay, and A. Paul, *J. Mater. Sci. Lett*. **6**, 1395 (1987).
14. R. C. Garvie, R. H. J. Hannink, and R. T. Pascoe, *Nature* **258**, 703 (1975).
15. D. -J. Kim, *J. Am. Ceram. Soc.* **73**, 115 (1990).
16. J. Chevalier, S. Deville, E. Munch, R. Jullian, and F. Lair, *Biomater.* **25**, 5539 (2004).
17. F. Sanchez-Bajo, F. L. Cumbrera, F. Guibertau, and A. Dominguez-Rodriguez, *Mater. Lett.* **15**, 39 (1992).
18. S. Selvasekarapandian, M. S. Bhuvaneswari, M. Vijayakumar, C. S. Ramya, and P. C. Angelo, *J. Eur. Ceram. Soc*. **25**, 2573 (2005).
19. V. Menvie Bekale, C. Legros, C. Haut, G. Sattonnay, and A. M. Huntz, *Solid State Ionics* **177**, 3339 (2006).
20. V. Ramaswamy, M. Bhagwat, D. Srinivas, and A. V. Ramaswamy, *Catal. Today* **97**, 63 (2004).
21. S. P. Ray and V. S. Stubican, *Mater. Res. Bull.* **12**, 549 (1977).
22. M. H. Maneshian and M. K. Banerjee, *J. Alloy. Compd.* **459**, 531 (2008).
23. F. Meschke, N. Claussen, G. De Portu, and J. Rodel, *J. Eur. Ceram. Soc.* **17**, 843 (1997).
24. R. R. Hughan and R. H. J. Hannink, *J. Am. Ceram. Soc.* **69**, 556 (1986).
25. A. A. Steffen, R. H. Dauskardt, and R. O. Ritchie, *J. Am. Ceram. Soc.* **74**, 1259 (1991).
26. R. H. J. Hannink, *J. Mater. Sci.* **18**, 457 (1983).
27. V. Thakare, *Int. J. Eng. Res. Develop*. **5**, 25 (2012).
28. C. Suryanarayana, *Mechanical alloying and milling*, 1st ed., CRC Press, Taylor and Francis, Boca Raton (2004). *Prog. Mater. Sci*. **46**, 1 (2001).
29. W. H. Hall and G. K. Williamson, *Proc. Phys. Soc.* **64B**, 937 (1951).
30. International Centre for Diffraction Data, JCPDS Powder Diffraction File, Card numbers, 13-307
31. International Centre for Diffraction Data, JCPDS Powder Diffraction File, Card number, 17-923
32. A. Sharma, *Mater Sci. Appl*. **4**, 504 (2013).
33. Y. L Chen and D. Z. Yang, *Ser. Met.* **29**, 1349 (1993).
34. Y. L. Chen, M. Qi, J. S. Wu, Wang, D. Z. Yang, and M. Stubičan, *Appl. Phys. Lett*. **65**, 303 (1994).
35. V. E. Annamalai, B. L. Anantharamu, C. V. Gokularathnam, and R. Krislmamurthy, *J. Mater. Sci. Lett.* **10**, 1373 (1991).
36. P. F. Becher and M. V. Swain, *J. Am. Ceram. Soc*. **75**, 493 (1992).
37. D. G. Lamas, G. E. Lascalea, and N. E. Walsoe De Reca, *J. Eur. Ceram. Soc*. **18**, 1217 (1998).
38. J. E. Bailey, D. Lewis, Z. M. Librant, and L. J. Porter, *Transactions J. British Ceram. Soc.* **71**, 25 (1972).
39. N. Gorodylova, Z. Dohnalova, and P. Sulcova, *Adv. Sci. Tech.* **87**, 6 (2014).
40. R. C. Garvie, *J. Phys. Chem.* **69**, 1238 (1965).
41. D. T. Livey and P. Murray, *Atom. Energy Res. Estab. (Gt. Brit.)* **1846**, 21 (1956).
42. E. D. Whitney, *J. Amer. Ceram. Soc.* **45**, 612 (1962).
43. G. Teufer, *Acta Cryst.* **15**, 1187 (1962).
44. J. D. McCullough and K. N. Trueblood, *Acta Cryst.* **12**, 507

(1959).
45. R. N. Patil and E. C. Subbarao, *Acta. Cryst. A* **26**, 535 (1970).
46. S. Fabris, A. T. Paxton, and M. W. Finnis, *Acta Mater.* **50**, 5171 (2002).
47. S. Nath, S. Bajaj, and B. Basu, *Int. J. Appl. Ceram. Technol.* **2**, 1 (2008).